Published in final edited form as:

ACS Sens. 2025 November 28; 10(11): 8395–8410. doi:10.1021/acssensors.5c01748.

Modulating chromophore flexibility in GEVIs through threonine-based molecular switches reveals an influence of membrane curvature on protein activity

Lee Min Leong[1,6,*], **Sang Chul Shin**[2,*], **Nazarii Frankiv**[1,3], **Jun Kyu Rhee**[1], **Heejung Kim**[4,5], **Jihye Seong**[5], **Junhyuk Woo**[1], **Kyungreem Han**[1], **Douglas Storace**[6], **Bradley J. Baker**[1,3]

[1]·Brain Science Institute, Korea Institute of Science and Technology, Seoul, Republic of Korea

[2]·Technological Convergence Center, Korea Institute of Science and Technology, Republic of Korea

[3]·Division of Bio-Medical Science and Technology, KIST School, Korea University of Science and Technology (UST), Seoul, South Korea

[4]·Department of Converging Science and Technology, Kyung Hee University, Seoul, Republic of Korea

[5]·Department of Pharmacology, Seoul National University College of Medicine, Seoul, Republic of Korea

[6]·Department of Biological Science, Florida State University, Tallahassee, Florida

Abstract

Many genetically encoded voltage indicators (GEVIs) rely on fluorescent protein (FP) domains to report changes in membrane potential. Rapid and reversible disruption of steady-state fluorescence during voltage sensor activation revealed transient conformational changes near the chromophore in the FP domain, implicating chromophore flexibility as a potential mechanism of signal modulation. Substitution of a bulky phenylalanine near the chromophore with threonine (F165T) introduced a distinct secondary component in the fluorescence response, consistent with increased chromophore mobility. This effect was tunable: an external, directionally polarized offset (164T/166F) reoriented the internal threonine side chain, restoring steric hindrance and eliminating the secondary signal. Thus, threonine can function as a context-sensitive molecular switch shaped by β-can surface chemistry. A second internal threonine (T203) also acted as a molecular switch under modified external conditions, generating a secondary signal that is susceptible to membrane curvature during depolarization suggesting that plasma membrane geometry can modulate GEVI activity under permissive conformational states. Crystal structures of Super Ecliptic pHluorin (SE), SE A227D, and a new FP variant revealed that external residues can influence internal side chain orientation. In the new variant, pH-dependent rearrangement of the seventh β-strand dramatically repositions D147 from the interior interacting with the chromophore to the external surface, while H148 shifts from the exterior to interact with the chromophore in alkaline

[*]These authors contributed equally to this submission

Author Contributions: L.M.L. and S.C.S. contributed equally to this work.

Notes: The authors declare no competing financial interest.

conditions. These insights led to the development of a new GEVI, Ulla, which inverts the polarity of the optical signal becoming brighter upon depolarization displays reduced pH sensitivity in the physiological range, and performs reliably under low-light, high-speed imaging conditions in vitro and in vivo using widefield and 2-photon microscopy. Together, these findings present a new approach to modulating chromophore behavior offering broad potential for FP-based biosensor development.

Keywords

genetically encoded voltage indicators (GEVIs); chromophore flexibility; threonine molecular switch; membrane curvature sensing; fluorescent protein biosensors

INTRODUCTION

Genetically encoded fluorescent biosensors require multiple fluorescent states to optically report changes in environmental conditions. For biosensors derived from fluorescent proteins (FP), sensitivity to the environment poses an intriguing challenge due to the architecture of the protein. FPs consist of an 11 β-sheet can structure that surrounds an internal chromophore. This layout protects the chromophore from the aqueous environment that would quench the fluorescence and provides support to minimize the flexibility of the chromophore. The internal environment surrounding the chromophore is therefore relatively stable consisting of a hydrogen bond network between the chromophore and the β-can structure as well as Van der Waal forces providing steric hindrance to hinder chromophore twisting.1,2 FP-based biosensors must therefore possess a mechanism for external environmental conditions to disrupt the internal environment of the chromophore in a consistent and reversible manner. Engineering improved biosensors would benefit from a better understanding of the mechanisms responsible for fluorescence transitions. The ArcLight-family of genetically encoded voltage indicators (GEVIs) is an excellent model system for interrogating the mechanisms mediating optical transitions of the FP since fluorescence can be rapidly and reversibly modulated by manipulating the plasma membrane potential.3–5 The Arc-Light-family of GEVIs consists of a voltage-sensing domain (VSD) spanning the plasma membrane fused to the pH-sensitive FP, Super Ecliptic pHluorin (SE)6,7 (Figure 1A). With the FP domain residing in the cytoplasm outside of the voltage field, the voltage-dependent optical signal of the GEVI is not reacting to voltage directly but is instead a response to the conformational change of the VSD. The VSD in ArcLight is from the voltage-sensing phosphatase gene family8 that has been shown to dimerize.9 This dimerization enables an interaction between the cytosolic FP domains10 which is altered when the VSD responds to a voltage transient.

A key modification that enhances ArcLight's voltage sensitivity more than 15-fold is the substitution of alanine with aspartic acid at position 227 (A227D numbering throughout refers to position in the FP) on the surface of the β-can of the FP domain.3 This externally positioned negative charge appears to act as a mediator, influencing the fluorescence of an adjacent FP domain within the dimer when the VSD responds to membrane potential transients. This intermolecular hypothesis implies the existence of a corresponding external

site on the neighboring FP domain that responds to changes in the electrostatic environment and relays this signal to the internal chromophore, ultimately modulating its fluorescence.

To investigate this interdomain interaction, we crystallized SE, SE A227D, and a novel mutant under four pH conditions to explore potential conformational changes associated with fluorescence transitions. Structural comparisons and targeted mutagenesis revealed that external amino acids on one side of a β-strand can influence the orientation of internal residues on the opposing side. In particular, specific internal threonine side chains can act as conformational switches. These threonines do not respond directly to voltage, but their side chain orientation can alternate between steric hindrance (via the methyl group) and potential hydrogen bonding (via the hydroxyl group) dependent upon the flanking chemistry-thereby regulating chromophore flexibility and fluorescent behavior.

By leveraging these threonine-based conformational switches, we developed a modified GEVI that inverts the voltage-dependent fluorescence response, becoming brighter during membrane depolarization. In addition to this signal polarity inversion, we observed that chromophore flexibility as inferred from altered fluorescence transition dynamics was further influenced by plasma membrane curvature, suggesting an unanticipated link between protein function and membrane geometry.

MATERIALS AND METHODS

Plasmid Design and Construction.

The Triple Mutant GEVI is described in Piao et al., 2015.4 The ArcLight construct is described in Jin et al., 2012.3 Primers were designed to introduce point mutations to the FP domain as required. Conventional one-step and two-step PCR were used to generate the target inserts. The inserts were cloned into the vector using NEB restriction enzymes. The backbone vector used in this study is pcDNA3.1 (Invitrogen, USA) with a CMV promoter.

Cell Culture and Transfection.

HEK 293 cells were cultured in Dulbecco’s Modified Eagle Medium (DMEM; Gibco, USA) supplemented with 10% Fetal Bovine Serum (FBS; Gibco, USA) in a 37 °C, 100% humidity and 5% CO2. For transfection, HEK 293 cells were suspended using 0.25% Trypsin-EDTA (Gibco, USA) then plated onto poly-L-lysine (Sigma-Aldrich, USA) coated #0 coverslips (0.08–0.13 mm thick and 10 mm diameter; Ted Pella, USA) at 70% confluency. Transient transfection was carried out with Lipofectamine 2000 (Invitrogen, USA) according to the manufacturer’s protocol.

Electrophysiology.

Coverslips with transiently transfected cells were inserted into a patch chamber (Warner instruments, USA) sealed with a #0 thickness cover glass for simultaneous voltage clamp and fluorescence imaging. The chamber was kept at 34 °C throughout the experiment and perfused with extracellular solution (150 mM NaCl, 4 mM KCl, 1 mM MgCl2, 2 mM CaCl2, 5 mM D-glucose and 5 mM HEPES, pH = 7.4). Filamented glass capillary tubes (1.5 mm/0.84 mm; World Precision Instruments, USA) were pulled by a micropipette puller

(Sutter, USA) prior to each experiment to pipet resistances of 3–5 MΩ for HEK 293 cells. The pipettes were filled with intracellular solution (120 mM K-aspartate, 4 mM NaCl, 4 mM MgCl2, 1 mM CaCl2, 10 mM EGTA, 3 mM Na2ATP and 5 mM HEPES, pH = 7.2) and held by a pipet holder (HEKA, Germany) mounted on a micromanipulator (Scientifica, UK). Whole cell voltage clamp and current clamp recordings of transfected cells were conducted using a patch clamp amplifier (HEKA, Germany).

Fluorescence Microscopy of Cultured Cells.

An inverted microscope (IX71; Olympus, Japan) equipped with a 60X oil-immersion lens, 1.35-numerical aperture (NA), was used for epifluorescence imaging. The light source was a 75 W xenon arc lamp (Osram, Germany) placed in a lamp housing (Cairn, UK). GFP was imaged using a filter cube consisting of an excitation filter (FF02-472/30-25), a dichroic mirror (FF495-Di03) and an emission filter (FF01-496) for the 470 nm wavelength excitation all from Semrock (USA). Two cameras were mounted on the microscope through a dual port camera adapter (Olympus, Japan). A slow speed, color charge-coupled-device (CCD) camera (Hitachi, Japan) was used to visualize cells during patch clamp experiments. Fluorescence changes of the voltage indicators were typically recorded at 1 kHz frame rate by a high-speed CCD camera (RedShirtImaging, USA). All the relevant optical devices were placed on a vibration isolation platform (Kinetic systems, USA) to avoid any vibrational noise during patch clamp fluorometry experiments.

Optical Data Acquisition and Analysis.

Resulting images from patch clamp fluorometry were acquired and analyzed for initial parameters such as fluorescence change, $\Delta F = Fx - F0$ (Fx being the fluorescence during frame x, and F0 being the average fluorescence of the first five frames of the recording) or fractional fluorescence change values ($\Delta F/F = ((Fx - F0)/F0) * 100$) by NeuroPlex (RedShirtImaging, USA) and Microsoft Excel (Microsoft, USA). The acquired data from whole cell voltage clamp experiments of HEK 293 cells were averages of 4 trials each trial consisting of 4 repetitions totaling 16 repetitions (technical replication) unless otherwise noted. The number of recorded cells in this work is biological replicates and the number of trials averaged for each HEK 293 cell should be interpreted as technical replication. Data were collected from recorded cells that did not lose their seals during the whole cell voltage clamp recording. ΔF/F values for the tested voltage pulses were plotted in OriginPro 2016 (OriginLab, USA). A ΔF/F trace versus time graph for each cell was also fitted for either double or single exponential decay functions in OriginPro 2016 as described previously.4 For membrane curvature comparisons, regions of interest (ROIs) correlating with more curved regions of an individual cell were compared to ROIs of less curved membrane regions of the same cell. The fluorescence trace starting 40 ms after the depolarization step until 1 ms before the membrane was repolarized to the holding potential (60 frames total) was fit to a linear slope $y = mx + b$ for each ROI for each of the four trials performed on the cell. The average of the slopes for each cell was tested for statistical significance via a TwoWay ANOVA Scheffe test.

Protein Expression and Purification.

The SE, SE A227D, and Ulla proteins were expressed by induction with 0.1 mM IPTG at 18 °C overnight in E. coli BL21 cells. Cells were harvested by centrifugation and resuspended in buffer containing 20 mM HEPES (pH 7.5), 150 mM NaCl, 2 mM β-mercaptoethanol, and were disrupted by sonication, and the crude lysate was centrifuged at 18,000 rpm (Hanil Supra 22K) for 40 min at 4 °C and the cell debris was discarded. The supernatant was loaded onto a nickel-chelated Hi-trap column (GE Healthcare) and eluted with a linear gradient of 25–500 mM imidazole in 20 mM HEPES (pH 7.5), 150 mM NaCl. The pooled fraction was further purified by gel filtration chromatography on HiLoad 26/60 Superdex-75 (GE Healthcare) pre-equilibrated with 20 mM HEPES (pH 7.5), 150 mM NaCl, and 2 mM DTT. The purity of the proteins at each stage was checked on 15% SDS-PAGE. The purified SE, SE A227D, and Ulla proteins were concentrated to 35–50 mg/mL using a VIVASPIN20 (Sartorius) concentrator and stored at −80 °C until use.

Crystallization, Diffraction Data Collection and Processing.

To obtain pH-variation of the SE crystal, purified SE was equilibrated in 20 mM HEPES (pH 7.5), 150 mM NaCl, and 2 mM DTT at 4 °C for 2 h prior to the crystallization attempts. The acid conditions of SE crystals were obtained by mixing an equal volume of the protein solution and a reservoir solution of 0.1 M sodium acetate (pH 4.5–6.5) and 2.2 M sodium chloride. The neutral conditions of SE crystals were obtained by mixing an equal volume of the protein solution and a reservoir solution of 0.1 M HEPES (pH 6.5–8.0), 2.5 M sodium chloride, 12% PEG 1500 and 2.2 M sodium chloride. The basic conditions of SE crystals were obtained by mixing an equal volume of the protein solution and a reservoir solution of 0.1 M sodium Tris (pH 8.0–9.5) and 0.8 M sodium dihydrogen phosphate. The acid conditions of SE A227D crystals were obtained by mixing an equal volume of the protein solution and a reservoir solution of 0.1 M citric acid (pH 4.5–6.0) and 20% (w/v) PEG 6000. The neutral conditions of SE A227D crystals were obtained by mixing an equal volume of the protein solution and a reservoir solution of 0.1 M Tris (pH 6.0–8.0), 0.2 M lithium chloride and 20% PEG 6000. The basic conditions of SE A227D crystals were obtained by mixing an equal volume of the protein solution and a reservoir solution of 0.1 M CHES (pH 8.0–9.5), 0.2 M sodium chloride and 1.26 M ammonium sulfate. The acid conditions of Ulla crystals were obtained by mixing an equal volume of the protein solution and a reservoir solution of 0.1 M acetate (pH 4.5–6.5), 25% (w/v) PEG 1500 and 30% (w/v) MPD. The neutral conditions of Ulla crystals were obtained by mixing an equal volume of the protein solution and a reservoir solution of 0.1 M imidazole (pH 6.5–8.0), 40% (w/v) isopropanol and 15% (w/v) PEG 8000. The basic conditions of Ulla crystals were obtained by mixing an equal volume of the protein solution and a reservoir solution of 0.1 M Tris (pH 8.0–9.5), 0.1 M magnesium chloride and 25% (w/v) PEG3350. Suitable crystals for X-ray diffraction were grown within 5–7 days. They were cryo-protected using the reservoir solution supplemented with 20% (w/v) additional glycerol, ethylene glycol (w/v) and were flash-frozen in liquid nitrogen. Diffraction data were collected at −173 °C using the beamline BL-5C equipped with an ADSC Quantum 315r CCD detector of Pohang Light Source (Pohang, Korea). All data sets were processed and scaled using the program DENZO and SCALEPACK from the HKL2000 program suite.11

Structure Determination and Analysis.

The electron density map was obtained by the molecular replacement method with the PHENIX12 program using the crystal structure of GFP (PDB code: 5WWK) as a search model.13 The model building and refinement were performed with Coot14 and PHENIX,12 respectively. The final models were validated using PROCHECK.15 The structure figure was visualized with PyMOL. Supplementary Table 2 summarizes statistics on the data collection and refinement.

Slice Imaging in Dorsal Hippocampal CA1 Region.

Virus injection and slice preparation were done according to an approved animal experiment protocol by the Institutional Animal Care and Use Committee at KIST (animal protocol 2019-099). 4 Week-old C57BL/6N male mice were anesthetized by 1.5%–3% isoflurane. Adeno-associated virus (AAV) AAV2/1-hSyn-Ulla was then injected into the CA1 region of the hippocampus bilaterally as described previously.16 Recordings were performed at least 2 weeks after the injection. 300 mm thick acute coronal brain slices were prepared following the NMDG protective recovery method.17 Halothane (Sigma, USA) was used to anesthetize the mice before euthanasia. The isolated mouse brain was sliced in ice-cold high-sucrose artificial cerebrospinal fluid (ACSF) solution (75 mM sucrose, 25 mM $NaHCO_3$, 2.5 mM KCl, 0.5 mM $CaCl_2$, 7 mM $MgCl_2$, 1.25 mM NaH_2PO_4, 87 mM NaCl and 25 mM D-glucose) gassed with 95% O_2/5% CO_2 to give a pH of 7.4 using the VT-1200 Vibratome (Leica, Germany). Slices were then allowed to recover for at least an hour in a chamber filled with ACSF, incubated at 36 °C. Coronal slices of BL6 mouse brain injected with AAV2/1-hSyn-Ulla 2 weeks prior to the experiment were prepared following the NMDG protective recovery method, and the dorsal hippocampal CA1 region of the BL6 mouse expressing Ulla was imaged during a Schaffer collateral stimulation using bipolar electrodes (FHC, Bowdoin, ME). Brain slice recordings were carried out at 33 °C with the recording chamber continuously perfused with ACSF. The stimulus timing trigger and recording were done using Multiclamp 700B amplifier (Molecular devices, USA). Each Ulla recording was either acquired at 1 kHz as 80 pixel × 80 pixel or at 5 kHz as 26 pixel × 26 pixel fluorescence intensity time-lapse images using an upright epifluorescence microscope (Slicescope, Scientifica, East Sussex, UK) equipped with a High-speed CCD camera (Neuro CCD, RedShirtImaging, Decatur, GA), a GFP filter set (GFP-3035D-OMF, Semrock, Rochester, NY), a 10× water immersion objective lens (UMPlanFL N; NA = 0.3, Olympus, Tokyo, Japan), and a 1.3 mW/cm2 460 nm LED light source (UHP-Mic-LED-460, Prizmatix, Givat-Shmuel, Israel). The fluorescence intensity trace of Ulla was low pass filtered offline using a 50 Hz fifth order Butterworth filter. The baseline prior to stimulation was used to apply an exponential decay curve. Traces represent a single recording or the averages of 5, 10, or 20 recordings were used to derive the Ulla response. The frame subtracted Ulla intensity images were pseudocolored by manually setting the colored intensity range from +0.3% $\Delta F/F$ to −0.2% $\Delta F/F$ and spatially low pass filtering with a 3 pixel × 3 pixel mean filter.

Surgical Procedures.

All experimental procedures were approved by the Florida State University ACUC. C57BL/6J adult male and female mice were anesthetized with ketamine/xylazine (90/10 mg/kg). Anesthetic depth was monitored during all surgical procedures via pedal reflex and a body temperature of 37.5C was maintained via a heating pad placed underneath the animal. Mice were given a preoperative dose of carprofen, dexamethasone, atropine and bupivacaine, and Lacrilube was applied to their eyes. For virus injections, an incision was made in the skin above the olfactory bulb, a small craniotomy was made and 500 nl of AAV2/1-hSyn-Ulla was injected into the olfactory bulb over a period of 15 min (Nanoject III, Drummond Scientific). Following completion of the injection, the incision was sutured and mice were administered postoperative doses of rimadyl for 3 days. A minimum of 2 weeks were allowed for Ulla expression before performing imaging experiments in which similar surgical procedures were used to attach a head-post to the skull using metabond (Parkell, Edgewood, NY). The skull above one or both olfactory bulbs was thinned and covered with cyanoacrylate to improve optical clarity or was removed and sealed with a glass coverslip.

In Vivo Imaging.

Imaging was carried out using a custom epifluorescence microscope built from Thorlabs (Newton, NJ) components with a 35 mm or 50 mm CCTV lens, or a 10 × 0.5 N.A. microscope objective. Illumination was provided by a Prizmatix LED (UHP-T-LED-455) filtered with a 488/10 nm (Semrock FF01-488/10). A dichroic mirror (59009bs, Chroma) directed the excitation light toward the preparation, and transmitted the fluorescence emission through a band-pass filter (Chroma 59009m), before being recorded using a DaVinci 1k camera (RedShirtImaging, Decatur, GA). Imaging was carried out between 40 and 200 Hz at a spatial resolution of 256 × 256 pixels. 2-Photon imaging was carried out on a Sutter Moveable Objective Microscope (MOM, Sutter Instruments) equipped with an 8 kHz scanner (Cambridge), GaAsP photomultiplier tubes (Hamamatsu), and a 2-photon optimized objective (10× 0.5 NA).18 A Spark Lasers ALCOR-920 provided 2-photon laser excitation which has an internal AOM to control its power. This system acquires images at 30.9 Hz at a spatial resolution of 512 × 512 pixels. During imaging experiments, mice were placed underneath the microscope objective during imaging with an odor delivery port placed in front of their nose. Olfactometer. The odor methyl valerate (CAS #624-24-8, Sigma-Aldrich) was presented to the animal using a custom flow-dilution olfactometer at concentrations between 1 and 10% of saturated vapor. The olfactometer design involved an odor stream at 28 mL/min that underwent an initial clean air dilution (30 mL/min). This odorized air flowed into a dual 3-way solenoid (360T041, NResearch, West Caldwell, NJ), which directed the flow to either an exhaust or a Teflon delivery manifold. Upon triggering the solenoid, the odor stream blended with a second air flow dilution (450 mL/min) in the delivery manifold which was in front of the animal's nose. An alternate design was used in a subset of the experiments in which the flow rates were controlled using mass flow controllers (Alicat, MC-100SCCM and MC-1 SLPM), and odors underwent only a single air dilution step.19–21 Respiration was measured in a subset of the preparations via a pressure sensor attached to the olfactometer odor delivery port.

Data Analysis.

Odorant-evoked signals were collected in consecutive trials separated by a minimum of 60 s. Ulla signals representing depolarization are shown as upward signals. Data from each pixel were low-pass Gaussian filtered between 2 and 4 Hz and had an exponential drift subtracted that was calculated based on the signal prior to the stimulus onset (exponential subtraction function in NeuroPlex). The signal from each pixel was divided by its resting fluorescence measured at the beginning of each trial. The fluorescence brightness analysis was measured by choosing a region of interest that captured the entire surface of the injected and uninjected hemibulbs. The mean fluorescence in the initial 2 s of the imaging trial was measured in both hemibulbs in 4 trials and averaged together. The results were normalized to the fluorescence in the uninjected hemibulb and averaged across all four preparations. The ΔF/F analysis was carried out by subtracting a 1 s window around the peak of the odor response from the 2 s immediately preceding the odor stimulus. This measurement was carried out in 4–5 trials per preparation before being averaged together. Measurements of Ulla time course dynamics were performed in regions of interest taken from the caudal-lateral olfactory bulb. The onset latency is defined as the time from the beginning of an inhalation to 63% of the peak ΔF/F. The offset latency is defined as the time from the peak ΔF/F to where the response reached 63% of the peak.

Custom software in MATLAB (Mathworks) and MView (Sutter Instruments) was used to spatially and temporally average the 2-photon imaging files (acquired at 512 × 512 pixels at 31 Hz) to 256 × 256 pixels and 7.8 Hz, respectively.20,21 The 2-photon imaging data were analyzed in spatially and temporally averaged files in which the pixel resolution was reduced to 256 × 256 and in which every 4 frames were averaged together to improve the signal-to-noise ratio using MATLAB (Mathworks) and MView (Sutter instruments). The 2-photon fluorescence traces were generated from an averaged file in which all single trials were aligned to the first inhalation following the odor command trigger. The in vivo 2-photon mean fluorescence is from the original 512 × 512 resolution data. All optical traces were generated from the spatially and temporally averaged files, although similar signals were observed in the raw data files. Data analysis was performed using Turbo-SM analysis software (SciMeasure, Decatur GA), and images were arranged using Adobe Illustrator (Adobe).

RESULTS

An Internal Conformational Change in the FP Domain Occurs During the Voltage-Dependent Fluorescence Transition. The interaction between neighboring fluorescent protein (FP) domains in ArcLight-derived GEVIs suggests that the A227D mutation introduces an external negative charge capable of modulating the fluorescence of an adjacent FP domain (Figure 1A). Previous work demonstrated that membrane depolarization alters the relationship between neighboring FP domains, as evidenced by voltage-dependent changes in intermolecular fluorescence resonance energy transfer (FRET) efficiency when cells cotransfected with ArcLight-CFP and ArcLight-YFP were subjected to voltage transients.10 In the ArcLight construct containing the SE A227D FP domain, manipulation

of membrane potential rapidly displaces the negative charge at position 227, potentially altering the electrostatic environment near a neighboring FP.

To identify FP regions capable of responding to an altered electrostatic environment, we crystallized SE and SE A227D under various pH conditions to reveal conformational changes that might underlie fluorescence modulation. SE is known to be highly pH-sensitive22 likely due to the orientation of the D147 side chain, which spans from the external surface of the β-can to the internal chromophore (Figure 1B). One oxygen atom of the D147 carboxylate group remains solvent-exposed, while the other forms a hydrogen bond with the chromophore. A similar conformation was recently observed in Lime, a derivative of SE with improved pH sensitivity.23 In contrast, EGFP adopts a different orientation, with the hydroxyl group of S147 residing on the exterior of the protein.24

The positioning of D147 made it a plausible candidate for interacting with the A227D transmitter from a neighboring FP domain. To assess the role of D147, we introduced a series of substitutions at this position into an ArcLight-derived GEVI TM-SEa construct with improved kinetics4 and recorded their voltage-dependent fluorescence responses. In the main figure, we highlight three representative examples D147A, D147N, and D147Q to illustrate distinct patterns of behavior (Figure 1C). The D147A mutant retained a robust optical signal, arguing against a direct interaction between D147 in one FP domain and D227 in a neighboring FP domain. In contrast, D147Q produced a more conventional voltage-dependent optical response, whereas D147N yielded a complex transition pattern, suggesting that the orientation of the nitrogen-containing side chain influences chromophore transitions.

Additional substitutions, including positively charged residues such as D147K and D147R, are shown in Supplemental Figure S2. Interestingly, both of these mutations produced responses similar to D147N, reinforcing the idea that the presence and orientation of a nitrogen group at this site can drive alternative transition patterns. Together, these results indicate that while D147 substitutions preserve voltage-dependent fluorescence, the chemistry and orientation of the side chain strongly modulate the nature of the optical transitions.

Crystal structures of SE A227D at different pH levels revealed no major global conformational changes (Figure 1D; Supplemental Figure S1). However, local inspection near the chromophore revealed a hydrogen bond network in SE A227D similar to that of avGFP, with subtle differences. Notably, the seventh β-strand in SE A227D begins at residue V150 compared to avGFP, where the β-strand starts at H148. In SE A227D, H148 is externally exposed, enabling the D147 side chain to span from the β-can surface into the chromophore pocket. One oxygen from the D147 carboxylate replaces the water molecule found near the chromophore in avGFP and GFP(S65T). Interestingly, the proton wire from the chromophore to E222 (via D147 and S205) remains intact in SE A227D, despite the presence of the T65 residue in the chromophore. This contrasts with GFP(S65T), where the T65 mutation disrupts the orientation of E222 and the continuity of the proton wire.

One of the most informative observations from the SE A227D structures was the invariance of T203 orientation across pH conditions. In GFP(S65T), T203 undergoes a pH-dependent conformational change: at low pH, the hydroxyl group hydrogen-bonds with the seventh β-strand, whereas at high pH (pH 8.0), it rotates to interact with the chromophore.25,26 In contrast, in SE A227D, T203 maintains a rigid orientation, regardless of pH. This rigidity is notable in light of the mutations introduced during SE development S202F and Q204T6 which flank T203 and were previously implicated in ArcLight function.27

The identity of residue 203 is known to affect FP fluorescence properties: nonpolar substitutions tend to stabilize the protonated chromophore, while aromatic substitutions like T203Y red-shift the emission spectrum in yellow FPs.26,28,29 To explore how this position influences voltage-dependent kinetics, we expressed T203X mutants of TM-SE in HEK293 cells and evaluated their responses using whole-cell voltage clamp (Figure 1E). The T203Q mutant retained an optical signal similar to TM-SE, with a slightly faster onset (τ_on ≈ 7.8 ± 0.6 ms vs 9.5 ± 0.5 ms in WT). The T203N mutant, however, significantly slowed the optical transition, with a biexponential comprised of a fast component (τ_on ≈ 9.1 ± 0.7 ms; 56.6 ± 0.1% of total) and a slow component (τ_on ≈ 75.7 ± 5.8 ms). Recovery kinetics were also altered: T203Q showed a slightly faster return to baseline (fast τ_off ≈ 7.2 ± 0.2 ms), while T203N had a pronounced slow decay (τ_off ≈ 69.7 ± 6.2 ms; 38.0 ± 0.1% of total signal).

These kinetic effects, arising from modest side chain substitutions at residue 203, strongly support the existence of a voltage-triggered conformational change within the FP domain. The fact that such changes occur on the millisecond time scale and alter chromophore behavior suggests that internal flexibility within the FP can mediate the optical response to voltage transients.

Removing Steric Hindrance Enables Optical Detection of Chromophore Flexibility During Voltage-Dependent Fluorescence Transitions. A potential mechanism underlying voltage-dependent fluorescence changes in the FP domain is chromophore movement, which may be modulated by surrounding structural constraints. A relevant precedent is the pH-sensitive red-shifted FP Katushka.30 At pH 8.0, Katushka is bright and adopts a cis-chromophore configuration (Figure 2A). At pH 5.5, it becomes dim, with the chromophore shifting to a trans-configuration, stabilized by a hydrogen bond with the side chain of S158 located within the β-can structure. This reversible isomerization is key to its fluorescence modulation.

In SE A227D, the homologous position to S158 is occupied by a bulky phenylalanine residue (F165), which introduces significant steric hindrance (Figure 2A). This steric hindrance likely prevents the chromophore from undergoing a similar cis– trans transition or other configurational flexibility. We hypothesized that removing steric hindrance at this position might unmask latent conformational dynamics of the chromophore during voltage-induced transitions.

To test this, we introduced F165X mutations in the FP domain of TM-SE and expressed the resulting GEVIs in HEK293 cells. Voltage-dependent fluorescence responses were measured via whole-cell patch clamp (Figure 2B). Both F165S and F165T variants exhibited a

biphasic fluorescence response, including a slower secondary component during membrane depolarization (highlighted by arrows in Figure 2B). Interestingly, SE F165A also exhibited a slow-rising biphasic response, characterized by an initial decrease in fluorescence followed by a delayed secondary component. This slower component was not attributable to the hydroxyl group present in serine or threonine, as the F165A mutant lacking both steric bulk and hydroxyl functionality produced an even more pronounced secondary component. These results indicate that the slower component arises from increased chromophore flexibility, unmasked by loss of steric hindrance.

In contrast, the F165V mutant did not show the secondary fluorescence component. The presence of a methyl group at this position appears to be sufficient to restore steric restriction, preventing conformational flexibility of the chromophore. These findings suggest that residue size at position 165 directly governs the chromophore's ability to adopt alternative configurations in response to VSD-mediated conformational changes.

Interplay between External and Internal Side Chains of the β-Can Structure Enables Threonine to Act as a Molecular Switch Modulating Chromophore Stability. An intriguing observation from the F165X mutation experiments (Figure 2B) was that valine, despite having a similarly sized methyl group as threonine, was capable of suppressing the secondary fluorescence component, whereas threonine was not. This suggested that the threonine side chain can either allow or inhibit chromophore flexibility depending on its spatial configuration.

Given that T203 exhibited a rigid, pH-invariant orientation in SE A227D crystal structures (Figure 1D; Supplemental Figure S1), and that the external flanking residues F202 and T204 had been introduced during the development of SE,6 we speculated that the electrostatic offset or permittivity gradient created by these residues could influence the internal orientation of T203, or more relevant here, T165. If the local external environment of the β-can structure can dictate side chain orientation, internal threonines might serve as tunable molecular switches that modulate chromophore behavior.

To explore the potential of a molecular switch, we mutated the external residues flanking position 165 in the F165T construct, aiming to restore steric hindrance by influencing the orientation of the threonine side chain (Figure 2C). In the N164F/165T/K166T (FTT) configuration, the secondary fluorescence component persisted, suggesting that this arrangement did not effectively reposition the threonine methyl group. However, when we reversed the external permittivity offset using the N164T/165T/K166F (TTF) combination the secondary component was markedly reduced (Figure 2C), appearing in only 1 of 5 cells tested (Supplemental Figure S3).

This result supports the hypothesis that the relative polarity and spatial orientation of external β-strand residues can influence the rotameric state of internal threonine side chains, effectively tuning their ability to impose steric hindrance. In this context, threonine functions as a context-sensitive molecular switch: its side chain can restrict or permit chromophore flexibility based on its externally modulated orientation. This represents a novel mechanism

by which external β-can chemistry governs internal chromophore dynamics, adding an additional layer of structural and functional tunability to FP-based biosensors.

A Second Threonine Switch Reveals an Influence of Plasma Membrane Curvature on Protein Activity. The ability to modulate the orientation of the threonine side chain at position 165 suggested that other internal threonine residues might also function as molecular switches, provided that their side chain orientation could be externally influenced. Indeed, the rationale for modifying the F165T construct stemmed from the chemical composition flanking T203 in SE specifically F202 and T204.

To test whether T203 could also act as a conformational switch, we inverted the polarity of its flanking residues, generating the construct TM-SE F202T/T204F. This mutant exhibited location-dependent behavior within the plasma membrane (Figure 3). AlphaFold31 structural predictions of the T203 side chain in the F202T/T204F background suggested an altered orientation, in which the threonine hydroxyl group is positioned to potentially form a hydrogen bond with the chromophore (Figure 3A). When expressed in HEK293 cells, this construct displayed a secondary fluorescence component during voltage-dependent transitions qualitatively similar to that seen with the F165X (Figure 2) series but with distinct functional characteristics.

One distinction was that the magnitude of the secondary component increased progressively with the strength of the depolarizing voltage steps (Figure 3B), indicating a voltage-step–dependent amplification of the FP domain’s optical response. Importantly, this phenomenon reflects altered chromophore flexibility rather than a change in the intrinsic voltage dependence of the sensor, as further supported by the spatial variability of this response (Figure 3C).

Imaging allows direct comparison of frames immediately before a voltage step with those captured during the early and late phases, as well as after repolarization, to pinpoint where signal differences occur within the cell. During the 200 mV depolarization step, the entire plasma membrane initially dimmed, but curved regions subsequently developed a steeper secondary component, driving fluorescence above prestimulus levels. This secondary component also decayed more slowly, enabling resolution of regions of interest (ROIs) where the GEVI behaved differently consistently corresponding to more highly curved areas of the plasma membrane (Figures 3C and Supplemental Figure S4).

Because membrane curvature cannot be precisely controlled at the cellular level, ROIs from curved and less-curved regions of the same cell were compared. The traces in Figure 3C are color-coded to their respective ROIs and represent the average of four trials, each consisting of four repetitions of the command voltage (black trace). For each trial, the slope of the secondary component was quantified by fitting the fluorescence trace from 40 ms after the depolarization step until 1 ms before repolarization to a linear function ($y = mx + b$). Across cells expressing the SE F202T/T204F construct, the slopes were consistently steeper in more curved regions (Figure 3C), a pattern observed in all five cells tested (Supplemental Figure S4).

In contrast, curvature-dependent modulation was not detected in the F165X constructs (Figure 3D), underscoring that the side chain environments at positions 165 and 203 confer qualitatively different modes of chromophore flexibility. For example, the F165A mutant exhibited a uniform secondary signal throughout the membrane for all cells tested (Supplemental Figure S5), while the N164T/165T/K166F construct (which reintroduced steric hindrance at position 165) also displayed a uniform response in four of five cells (Supplemental Figure S3). Interestingly, in one cell, a secondary component emerged specifically in curved regions, suggesting that the 164T/165T/K166F mutant has reduced sensitivity to curvature.

Finally, while the original GEVI construct (TM-SE) typically lacked a secondary component during voltage transients, occasional exceptions were observed (Supplemental Figure S6). While these findings suggest a curvature-dependent modulation of the GEVI response, we note that other factors such as local lipid composition,32 membrane tension,33 cytoskeletal interactions,34 or even subtle differences in voltage-sensing domain conformational change at curved regions similar to mechanosensitive channels35 may also contribute.

Side Chain Charge at the External 204 Position in the FP Domain Inverts the Voltage-Dependent Optical Signal. The internal threonine switches at F165 and T203 revealed distinct secondary components, indicating that chromophore flexibility can generate functionally different optical transitions. To further probe this mechanism, we tested the effect of mutating a neighboring external residue position 204 located on the surface of the β-can adjacent to T203.

Substitutions at T204 demonstrated that side chain charge and polarity strongly influence the FP domain's optical response (Figure 4A). Introducing a negative charge at this position inverted the polarity of the voltage-dependent signal: the T204D mutant produced a modest inversion, while T204E showed a robust +9% ΔF/F in response to a 200 mV depolarization. In contrast, the T204K mutant produced only a small 3% dimming, with a biphasic response a fast decrease in fluorescence followed by a slower increase similar to that seen with the F165T construct (Figure 2).

Notably, T204Q and T204K also displayed curvature-sensitive secondary components during depolarization of the plasma membrane. In HEK293 cells, both mutants exhibited enhanced fluorescence transitions in curved regions of the membrane, while flatter regions showed little detectable secondary component (Figure 4B). This pattern was more consistent for cells expressing T204K (Supplemental Figure S7) than T204Q (Supplemental Figure S8). By contrast, the T204N mutant displayed a more uniform optical response across the membrane, with little to no detectable curvature sensitivity in any of the cells tested (Supplemental Figure S8).

These findings indicate that external charge and polarity at position 204 not only modulate the voltage-dependent optical response but can also impart curvature sensitivity, likely by influencing the conformational flexibility of neighboring internal residues. The diversity of behaviors observed across T204X mutants suggests that substitutions at this external site affect the chromophore indirectly, potentially by altering the rotameric state of adjacent

residues such as T203. Together, these results support a model in which side chain-mediated configurational flexibility determines whether conformational shifts of the FP Domain triggered by VSD activation can sufficiently perturb the chromophore to elicit a secondary fluorescence transition. Thus, curvature sensitivity appears to depend upon the dynamic flexibility of the chromophore environment.

Repositioning the External Negative Charge Along the 11th β-Strand Yields a Novel GEVI, Ulla, with an Inverted Voltage Signal and Altered pH Sensitivity. One particularly striking feature of the T204X mutants was the inversion of the voltage-dependent optical signal when the side chain carried a negative charge (Figure 4A). A GEVI that brightens during depolarization may offer advantages for in vivo imaging, where an increase in fluorescence could enhance the detection of active cells against a dimmer, nonactive background.

To optimize this inverted optical signal, we focused on enhancing the performance of the T204E mutant by re-evaluating the position of the external negative charge originally introduced at position A227D. While previous efforts to relocate this charge along the FP surface had not improved the signal strength in ArcLight derivatives36 we reasoned that the altered surface chemistry in T204E might enable synergistic effects.

We reverted the D227 back to alanine and performed an aspartic acid scan of the remaining external residues along the 11th β-strand (Figure 5A). This screen revealed that placing the negative charge at position F223 in combination with T204E more than doubled the dynamic fluorescence response. The resulting GEVI, T204E/F223D, produced a >25% ΔF/F signal in response to a 100 mV depolarization, with the fluorescence increasing upon depolarization. We named this construct Ulla, the Korean word for “ascend.”

In addition to its inverted voltage polarity, Ulla also displayed reduced pH sensitivity within the physiological range. To quantify this, we expressed and purified the FP domains of Ulla, the original Super Ecliptic pHluorin (SE), and SE A227D (from ArcLight) and measured their fluorescence responses across a range of pH values (Figure 5B). All three variants showed increased fluorescence at higher pH values. The original SE and SE A227D had nearly identical pKa values (7.2 and 7.3, respectively). However, Ulla exhibited a significantly shifted pKa of 8.2, a full pH unit more alkaline. Notably, Ulla differs from SE by only two surface mutations (T204E and F223D), yet this modest change yielded a substantial reduction in physiological pH sensitivity. Thus, Ulla integrates a voltage signal that brightens during depolarization with a pH profile that minimizes interference from normal cellular fluctuations providing a new GEVI platform optimized for improved imaging performance in live cells and tissues.

Crystal Structures of the Ulla FP Domain Reveal a pH-Induced Shift in the Seventh β-Strand and a Threonine Switch at Position 203. The ability to control the threonine switch at position 165 (Figure 2) was initially inspired by the flanking mutations F202 and T204 found in the original SE protein (Figure 1) Given that Ulla contains a mutation at position 204 and displays an altered pKa, we solved crystal structures of the Ulla FP domain (SE T204E/F223D) under different pH conditions (Figure 5B) and compared them to the original SE structures (Figure 5C). Unlike SE and SE A227D, Ulla exhibits two

notable conformational changes in response to pH. First, at pH 6.0, D147 interacts with the chromophore in a configuration similar to SE and SE A227D (Figure 5C and Supplemental Figure S1). However, at pH 8.5, the seventh β-strand extends, repositioning the D147 side chain completely to the external surface of the β-can. In this conformation, a water molecule occupies the site vacated by the D147 carboxylate, preserving the hydrogen bond network with the chromophore. Interestingly, one of the four monomers in the Ulla pH 8.5 structure retains D147 in its internal orientation, suggesting structural heterogeneity near the protein's pKa a phenomenon consistent with dynamic equilibrium between states (see PDB: 8JLU).

The second conformational change involves T203, providing structural evidence in addition to the functional evidence in Figure 2 for an internal threonine side chain acting as a conformational switch. In SE and SE A227D, the T203 hydroxyl group remains oriented toward a bridging water molecule between the seventh and 10th β-strands, helping stabilize the β-can structure (Figure 5C). Across pH 6.0 to 8.5, the positions of the chromophore, D147, T203, and S205 in SE remain essentially invariant.

In contrast, T203 in Ulla adopts multiple conformations depending on pH. At low pH, T203 orients toward the internal oxygen of D147, enabling a new hydrogen bond not present in SE. At pH 7.0, two distinct orientations are observed for the T203 side chain, while at pH 8.5, T203 exhibits multiple rotameric states, including conformations that allow direct interaction with the chromophore. These pH-dependent structural changes in T203 support the idea that external residue mutations at T204 indirectly influence internal chromophore-adjacent side chains, modulating their flexibility and function.

Despite this enhanced internal flexibility, Ulla exhibits photostability similar to ArcLight when expressed in HEK293 cells (Supplemental Figure S9), indicating that the conformational dynamics do not compromise the practical usability of the sensor.

Population Signals from the Novel GEVI, Ulla. While this is not the first GEVI to invert the polarity of the voltage-dependent optical signal, an indicator that becomes 25% brighter upon depolarization presents a promising new tool for monitoring activity in neuronal circuits. Indeed, alternate fluorescent responses by GEVIs to voltage can enable creative investigations of neuronal circuits.37 Despite advances, voltage imaging remains challenging, particularly due to the need for membrane-restricted probes and the high background fluorescence produced by densely interwoven neurites.38,39 A GEVI that increases in brightness upon depolarization could improve signal discrimination by lowering background in inactive regions, thereby enhancing contrast without requiring somatic expression restriction.

Ex Vivo Imaging in Mouse Hippocampus. To evaluate Ulla's performance in brain tissue, an AAV expressing Ulla under the human synapsin promoter was injected into the CA1 region of the mouse hippocampus (Figure 6A). Two weeks post-injection, acute brain slices were prepared and voltage-sensitive fluorescence was recorded during electrical stimulation of the Schaffer collaterals (Figure 6B,C). Upon stimulation, a rapid increase in fluorescence was observed, consistent with neuronal depolarization. This was followed by a decrease in fluorescence, reflecting network-level inhibition, a pattern previously observed in CA1 using

ArcLight.39,40 The excitatory component (~0.2% ΔF/F) was clearly detectable in single trials due to a robust signal-to-noise ratio (SNR ~20) (Figure 6C).

To assess Ulla's performance under lower light and faster imaging conditions, we repeated CA1 imaging at 5 kHz frame rates and reduced excitation power (Figure 6D). Even at 500 mW/cm2, single-trial detection remained possible (~0.2% ΔF/F, SNR = 2), and the signal quality improved with trial averaging. At higher illumination levels (13 W/cm2), single-trial SNR improved substantially, confirming that Ulla supports high-speed imaging at variable light levels.

In Vivo Imaging in the Olfactory Bulb. We next evaluated Ulla's in vivo functionality in the mouse olfactory bulb (OB), a model system with well-characterized sensory-evoked voltage signals. An adeno-associated virus (AAV) expressing Ulla was injected into the OB. The resulting fluorescence was subsequently monitored using widefield and 2-photon microscopy (Figure 6E). In all tested preparations, we observed, robust fluorescence in the injected hemibulb (Figure 6F, left), which was on average 2.2 ± 0.5 times brighter than the uninjected side (range: 1.85–3.02 fold, n = 4; p = 0.02, Wilcoxon rank-sum test). This confirms that Ulla expression is detectable above endogenous autofluorescence when performing in vivo imaging using widefield illumination. Presentation of the odorant methyl valerate (1–6% saturated vapor) elicited broad activity across the dorsal olfactory bulb in all tested animals (n = 9; Figure 6F, right). Spatially distinct temporal dynamics were observed in regions of interest measured in different locations across the OB. Regions of interest in the caudal-lateral bulb (ROI1) exhibited rhythmic oscillations that tracked respiration, returning most of the way to baseline between each sniff (Figure 6G, ROI1). In contrast, the rostral bulb exhibited a slower, sustained increase in fluorescence (Figure 6G, (ROI 2). These differences are consistent with prior measurements from the dorsal bulb using other sensors, and reliably tracked the duration of the odor presentation (Figure 6H).41–44 The mean odor-evoked response was 0.76 ± 0.28% ΔF/F (range: 0.38–1.07%, quantification performed in 3 animals, average of 4–5 trials per preparation). The time from the beginning of an inhalation to 63% of the peak ΔF/F was 69.3 ± 4.1 ms (range: 40–90 ms) and the time for the signal to decay to 63% of the peak ΔF/F was 72.7 ± 3.5 ms (range: 50–90 ms, quantification from 3 animals, averaged from a total of 15 trials, 5 trials per animal). Next, we tested whether Ulla could report odor-evoked activity in the olfactory bulb under 2-photon excitation in a subset of the preparations. Individual glomeruli were resolvable under 2-photon illumination (Figure 6I), and odor-triggered fluorescence changes were observed in each preparation (Figure 6J, N = 4 preparations, traces are the mean of 13 single trials aligned to respiration).

DISCUSSION

Chromophore stability has long been a prized feature in the development of fluorescent proteins (FPs). Bright, stable fluorescence underpins imaging applications ranging from cellular anatomy to protein localization and circuit connectivity. Biosensors, however, face an added demand: they must not only emit robust signals but also undergo reproducible changes in fluorescence in response to environmental stimuli. This creates a fundamental design challenge balancing chromophore stability with functional flexibility.

Too much flexibility leads to low fluorescence and signal loss, whereas too little prevents responsiveness. The ability to disrupt steady-state fluorescence through controlled changes in membrane potential has allowed us to optically probe transitions between states, providing insight into both the stability and accessibility of alternative fluorescent conformations within the FP domain.

Here, we document a novel mechanism to introduce conditional chromophore flexibility via a molecular switch, enabled by the structural duality of threonine. Its side chain features a hydrophobic methyl group and a hydrophilic hydroxyl group, allowing steric or hydrogen bonding interactions depending on its orientation. By substituting F165 (a bulky phenylalanine near the chromophore) with threonine, we created a more dynamic internal environment capable of supporting alternative side chain orientations. The resulting F165T construct displayed a secondary component in the fluorescence response to membrane depolarization an indicator of increased chromophore mobility (Figure 2).

Systematic mutagenesis showed that the size and shape of the side chain at position 165 modulated this secondary component. Alanine (F165A) amplified the secondary signal, while larger side chains (e.g., F165Y) eliminated it. Notably, valine (F165V), despite being similar in size to threonine, abolished the secondary component suggesting that precise side chain orientation, not size alone, governs the steric constraints on the chromophore.

We further demonstrated that the orientation of the threonine methyl group could be externally controlled by engineering a directional polarity offset in the flanking residues (Figure 2C). When the polarity offset was reversed, the secondary component was mostly inhibited strong evidence that threonine acts as a context-sensitive molecular switch.45–47 Importantly, the position of the threonine switch is also consequential. The F165 site offered an ideal testbed due to its relatively nonpolar environment and spatial tolerance for substitutions. In contrast, T203 occupies a more constrained internal context. In the crystal structures of SE and SE A227D, the T203 hydroxyl group is consistently oriented away from the chromophore, interacting instead with a bridging water molecule that stabilizes the β-can structure. Nonetheless, by inverting the external polarity flanking T203, we were able to induce a secondary component in the voltage-dependent optical signal (Figure 3), indicating that even native threonine residues, when subjected to an altered external environment, can function as molecular switches that modulate chromophore behavior.

Interestingly, T203-linked transitions were sensitive to membrane curvature, a property not shared by the F165X constructs. A similar curvature-dependent secondary component was observed for the T204Q and T204K mutants (Figure 4), while the T204N mutant, which maintained chromophore rigidity, did not exhibit this behavior. These findings suggest that curvature sensitivity emerges only under permissive conformational conditions when internal flexibility allows external perturbations (such as FP–FP repositioning) to affect the chromophore environment.

The enhanced secondary component observed in curved regions of the plasma membrane points to a geometry-dependent modulation of GEVI activity. However, membrane curvature is unlikely to be the sole determinant. Curved regions of the membrane are also associated

with distinct lipid compositions, altered membrane tension, and cytoskeletal remodeling, any of which could modify the environment of the FP or VSD and thereby influence optical signals. Moreover, it is possible that the conformational trajectory of the voltage-sensing domain itself is slightly altered in curved regions, subtly changing its coupling to the FP. Thus, while curvature provides a convenient and visually accessible correlate of these effects, our findings likely reflect the combined influence of multiple membrane-associated factors that are enriched or reorganized at curved surfaces. Thus, curvature exerts an observable influence on GEVI activity, but likely reflects a convergence of multiple membrane-associated factors rather than acting as an isolated determinant. Future experiments designed to disentangle these variables will be required to isolate the specific contribution of curvature.

The mechanism by which membrane curvature influences FP function remains unresolved. One hypothesis is that curvature modulates intermolecular interactions between dimerized GEVI molecules, altering the spatial arrangement of FP domains. Alternatively, curvature might affect the conformation or mobility of the VSD itself, indirectly repositioning FPs. Despite this uncertainty, these findings open the door to developing GEVIs capable of reporting not just voltage, but subtle differences in membrane morphology an exciting new dimension in voltage imaging.

Our data also reveal how external side chains can influence β-can secondary structure. In Ulla, the modified FP domain not only inverts the voltage-dependent signal but also undergoes a pH-dependent shift in the length of the seventh β-strand (Figure 5). At pH < pKa, D147 resides near the chromophore; above the pKa, the β-strand extends from V150 to H148, displacing D147 to the exterior and permitting H148 to interact with the chromophore. This shift introduces a novel mode of dynamic chromophore influence by environmental pH. This variation in β-strand length depending on external charge may well be the mechanism of the voltage-dependent optical response for the ArcLight-family of GEVIs. Such a mechanism would explain the inverted polarity of the voltage-dependent signal for Marina,48 another ArcLight-derived GEVI consisting of D147A and H148A mutations. Whether the repositioned negative charge at F223D in Ulla and the A227D in ArcLight can mediate a similar dynamic in the seventh β-strand of a neighboring FP domain will require further structural data of the dimerized protein.

The engineering of Ulla a GEVI that brightens during depolarization and has a shifted pH sensitivity illustrates how the principles described here can translate into practical biosensors. Ulla combines high signal contrast with compatibility for both low-light, high-speed imaging and in vivo applications. In hippocampal slices, it reported voltage transients at 5 kHz acquisition under minimal illumination (Figure 6D). In the mouse olfactory bulb, Ulla recorded odor-evoked responses using both widefield and two-photon microscopy (Figure 6F–J), without requiring somatic expression restriction.39 The single-trial SNR and response reproducibility were comparable to those reported with ArcLight49 validating Ulla’s utility in functional imaging using simple widefield setups.

Together, these results show that the disruption of steady-state fluorescence by membrane voltage can be used to reveal internal conformational dynamics in FPs. This study

demonstrates that side chain orientation in the β-can structure externally directed yet internally consequential can be harnessed to modulate chromophore behavior. Moreover, this structural flexibility allows the protein to exhibit location-dependent activity, influenced by both membrane potential and curvature.

In conclusion, fluorescent proteins offer not only a window into the cell, but a platform to explore and report complex interactions between protein structure and membrane environment, with unprecedented optical resolution.

Supplementary Material

Refer to Web version on PubMed Central for supplementary material.

Bibliography

(1). Martin ME; Negri F; Olivucci M Origin, nature, and fate of the fluorescent state of the green fluorescent protein chromophore at the CASPT2//CASSCF resolution. J. Am. Chem. Soc 2004, 126 (17), 5452–5464. [PubMed: 15113217]

(2). Park JW; Rhee YM Electric Field Keeps Chromophore Planar and Produces High Yield Fluorescence in Green Fluorescent Protein. J. Am. Chem. Soc 2016, 138 (41), 13619–13629. [PubMed: 27662359]

(3). Jin L; Han Z; Platisa J; Wooltorton JR; Cohen LB; Pieribone VA Single action potentials and subthreshold electrical events imaged in neurons with a fluorescent protein voltage probe. Neuron 2012, 75 (5), 779–785. [PubMed: 22958819]

(4). Piao HH; Rajakumar D; Kang BE; Kim EH; Baker BJ Combinatorial mutagenesis of the voltage-sensing domain enables the optical resolution of action potentials firing at 60 Hz by a genetically encoded fluorescent sensor of membrane potential. J. Neurosci 2015, 35 (1), 372–385. [PubMed: 25568129]

(5). Lee S; Geiller T; Jung A; Nakajima R; Song Y-K; Baker BJ Improving a genetically encoded voltage indicator by modifying the cytoplasmic charge composition. Sci. Rep 2017, 7 (1), 8286. [PubMed: 28811673]

(6). Miesenbock G; De Angelis DA; Rothman JE Visualizing secretion and synaptic transmission with pH-sensitive green fluorescent proteins. Nature 1998, 394 (6689), 192–195. [PubMed: 9671304]

(7). Ng M; Roorda RD; Lima SQ; Zemelman BV; Morcillo P; Miesenbock G Transmission of olfactory information between three populations of neurons in the antennal lobe of the fly. Neuron 2002, 36 (3), 463–474. [PubMed: 12408848]

(8). Murata Y; Iwasaki H; Sasaki M; Inaba K; Okamura Y Phosphoinositide phosphatase activity coupled to an intrinsic voltage sensor. Nature 2005, 435 (7046), 1239–1243. [PubMed: 15902207]

(9). Rayaprolu V; Royal P; Stengel K; Sandoz G; Kohout SC Dimerization of the voltage-sensing phosphatase controls its voltage-sensing and catalytic activity. J. Gen. Physiol 2018, 150 (5), 683–696. [PubMed: 29695412]

(10). Leong LM; Kang BE; Baker BJ Improving the flexibility of Genetically Encoded Voltage Indicators via intermolecular FRET. Biophys. J 2021, 120 (10), 1927–1941. [PubMed: 33744262]

(11). Otwinowski Z; Minor W Processing of X-ray diffraction data collected in oscillation mode. Methods Enzymol. 1997, 276, 307–326. [PubMed: 27754618]

(12). Adams PD; Afonine PV; Bunkoczi G; Chen VB; Davis IW; Echols N; Headd JJ; Hung LW; Kapral GJ; Grosse-Kunstleve RW; et al. PHENIX: a comprehensive Python-based system for macromolecular structure solution. Acta Crystallogr., Sect. D:Biol. Crystallogr 2010, 66 (2), 213–221. [PubMed: 20124702]

(13). Augustine G; Raghavan S; NumbiRamudu K; Easwaramoorthi S; Shanmugam G; Seetharani Murugaiyan J; Gunasekaran K; Govind C; Karunakaran V; Ayyadurai N Excited State Electronic Interconversion and Structural Transformation of Engineered Red-Emitting Green Fluorescent Protein Mutant. J. Phys. Chem. B 2019, 123 (10), 2316–2324. [PubMed: 30789731]

(14). Emsley P; Cowtan K Coot: model-building tools for molecular graphics. Acta Crystallogr., Sect. D:Biol. Crystallogr 2004, 60 (12), 2126–2132. [PubMed: 15572765]

(15). Laskowski RA; Moss DS; Thornton JM Main-chain bond lengths and bond angles in protein structures. J. Mol. Biol 1993, 231 (4), 1049–1067. [PubMed: 8515464]

(16). Lowery RL; Majewska AK Intracranial injection of adeno-associated viral vectors. J. Visualized Exp 2010, 45, 2140.

(17). Ting JT; Daigle TL; Chen Q; Feng G Acute brain slice methods for adult and aging animals: application of targeted patch clamp analysis and optogenetics. Methods Mol. Biol 2014, 1183, 221–242. [PubMed: 25023312]

(18). Yu CH; Yu Y; Adsit LM; Chang JT; Barchini J; Moberly AH; Benisty H; Kim J; Young BK; Heng K; et al. The Cousa objective: a long-working distance air objective for multiphoton imaging in vivo. Nat. Methods 2024, 21 (1), 132–141. [PubMed: 38129618]

(19). Williams E; Dewan A Olfactory Detection Thresholds for Primary Aliphatic Alcohols in Mice. Chem. Senses 2020, 45 (7), 513–521. [PubMed: 32609815]

(20). Leong L; Wharton D; Subramanian N; Karamched B; Bertram R; Storace DA Evidence that interglomerular inhibition generates non-monotonic concentration-response relationships in mitral/tufted glomeruli in the mouse olfactory bulb. bioRxiv 2025, DOI: 10.1101/2025.02.28.640652v2.

(21). Subramanian N; Leong LM; Salemi Mokri Boukani P; Storace DA Recent odor experience selectively modulates olfactory sensitivity across the glomerular output in the mouse olfactory bulb. Chem. Senses 2025, 50, bjae045. [PubMed: 39786438]

(22). Shen Y; Rosendale M; Campbell RE; Perrais D pHuji, a pH-sensitive red fluorescent protein for imaging of exo- and endocytosis. J. Cell Biol 2014, 207 (3), 419–432. [PubMed: 25385186]

(23). Shen Y; Wen Y; Sposini S; Vishwanath AA; Abdelfattah AS; Schreiter ER; Lemieux MJ; de Juan-Sanz J; Perrais D; Campbell RE Rational Engineering of an Improved Genetically Encoded pH Sensor Based on Superecliptic pHluorin. ACS Sens. 2023, 8 (8), 3014–3022. [PubMed: 37481776]

(24). Arpino JA; Rizkallah PJ; Jones DD Crystal structure of enhanced green fluorescent protein to 1.35 A resolution reveals alternative conformations for Glu222. PLoS One 2012, 7 (10), No. e47132. [PubMed: 23077555]

(25). Elsliger MA; Wachter RM; Hanson GT; Kallio K; Remington SJ Structural and spectral response of green fluorescent protein variants to changes in pH. Biochemistry 1999, 38 (17), 5296–5301. [PubMed: 10220315]

(26). Ormo M; Cubitt AB; Kallio K; Gross LA; Tsien RY; Remington SJ Crystal structure of the Aequorea victoria green fluorescent protein. Science 1996, 273 (5280), 1392–1395. [PubMed: 8703075]

(27). Han Z; Jin L; Chen F; Loturco JJ; Cohen LB; Bondar A; Lazar J; Pieribone VA Mechanistic studies of the genetically encoded fluorescent protein voltage probe ArcLight. PLoS One 2014, 9 (11), No. e113873. [PubMed: 25419571]

(28). Heim R; Prasher DC; Tsien RY Wavelength mutations and posttranslational autoxidation of green fluorescent protein. Proc. Natl. Acad. Sci. U.S.A 1994, 91 (26), 12501–12504. [PubMed: 7809066]

(29). Creemers TM; Lock AJ; Subramaniam V; Jovin TM; Volker S Photophysics and optical switching in green fluorescent protein mutants. Proc. Natl. Acad. Sci. U.S.A 2000, 97 (7), 2974–2978. [PubMed: 10716703]

(30). Pletneva NV; Pletnev VZ; Shemiakina II; Chudakov DM; Artemyev I; Wlodawer A; Dauter Z; Pletnev S Crystallographic study of red fluorescent protein eqFP578 and its far-red variant Katushka reveals opposite pH-induced isomerization of chromophore. Protein Sci. 2011, 20 (7), 1265–1274. [PubMed: 21563226]

(31). Abramson J; Adler J; Dunger J; Evans R; Green T; Pritzel A ; Ronneberger O; Willmore L; Ballard AJ; Bambrick J; et al. Accurate structure prediction of biomolecular interactions with AlphaFold 3. Nature 2024, 630 (8016), 493–500. [PubMed: 38718835]

(32). Sorre B; Callan-Jones A; Manneville JB; Nassoy P; Joanny JF; Prost J; Goud B; Bassereau P Curvature-driven lipid sorting needs proximity to a demixing point and is aided by proteins. Proc. Natl. Acad. Sci. U.S.A 2009, 106 (14), 5622–5626. [PubMed: 19304798]

(33). Kozlov MM; Chernomordik LV Membrane tension and membrane fusion. Curr. Opin. Struct. Biol 2015, 33, 61–67. [PubMed: 26282924]

(34). Kessels MM; Qualmann B Interplay between membrane curvature and the actin cytoskeleton. Curr. Opin. Cell Biol 2021, 68, 10–19. [PubMed: 32927373]

(35). Bavi O; Cox CD; Vossoughi M; Naghdabadi R; Jamali Y; Martinac B Influence of Global and Local Membrane Curvature on Mechanosensitive Ion Channels: A Finite Element Approach. Membr. 2016, 6 (1), 14.

(36). Kang BE; Leong LM; Kim Y; Miyazaki K; Ross WN; Baker BJ Mechanism of ArcLight derived GEVIs involves electrostatic interactions that can affect proton wires. Biophys. J 2021, 120 (10), 1916–1926. [PubMed: 33744263]

(37). Kannan M; Vasan G; Haziza S; Huang C; Chrapkiewicz R; Luo J; Cardin JA; Schnitzer MJ; Pieribone VA Dual-polarity voltage imaging of the concurrent dynamics of multiple neuron types. Science 2022, 378 (6619), No. eabm8797. [PubMed: 36378956]

(38). Rhee JK; Leong LM; Mukim MSI; Kang BE; Lee S; Bilbao-Broch L; Baker BJ Biophysical Parameters of GEVIs: Considerations for Imaging Voltage. Biophys. J 2020, 119, 1. [PubMed: 32521239]

(39). Nakajima R; Baker BJ Mapping of excitatory and inhibitory postsynaptic potentials of neuronal populations in hippocampal slices using the GEVI, ArcLight. J. Phys. D: Appl. Phys 2018, 51 (50), 504003. [PubMed: 30739956]

(40). Nakajima R; Laskaris N; Rhee JK; Baker BJ; Kosmidis EK GEVI cell-type specific labelling and a manifold learning approach provide evidence for lateral inhibition at the population level in the mouse hippocampal CA1 area. Eur. J. Neurosci 2021, 53 (9), 3019–3038. [PubMed: 33675122]

(41). Spors H; Grinvald A Spatio-temporal dynamics of odor representations in the mammalian olfactory bulb. Neuron 2002, 34 (2), 301–315. [PubMed: 11970871]

(42). Spors H; Wachowiak M; Cohen LB; Friedrich RW Temporal dynamics and latency patterns of receptor neuron input to the olfactory bulb. J. Neurosci 2006, 26 (4), 1247–1259. [PubMed: 16436612]

(43). Storace DA; Braubach OR; Jin L; Cohen LB; Sung U Monitoring brain activity with protein voltage and calcium sensors. Sci. Rep 2015, 5, 10212. [PubMed: 25970202]

(44). Platisa J; Zeng H; Madisen L; Cohen LB; Pieribone VA; Storace DA Voltage imaging in the olfactory bulb using transgenic mouse lines expressing the genetically encoded voltage indicator ArcLight. Sci. Rep 2022, 12 (1), 1875. [PubMed: 35115567]

(45). Agmon N Proton pathways in green fluorescence protein. Biophys. J 2005, 88 (4), 2452–2461. [PubMed: 15681647]

(46). Shinobu A; Palm GJ; Schierbeek AJ; Agmon N Visualizing proton antenna in a high-resolution green fluorescent protein structure. J. Am. Chem. Soc 2010, 132 (32), 11093–11102. [PubMed: 20698675]

(47). Shinobu A; Agmon N Proton Wire Dynamics in the Green Fluorescent Protein. J. Chem. Theory Comput 2017, 13 (1), 353–369. [PubMed: 28068768]

(48). Platisa J; Vasan G; Yang A; Pieribone VA Directed Evolution of Key Residues in Fluorescent Protein Inverses the Polarity of Voltage Sensitivity in the Genetically Encoded Indicator ArcLight. ACS Chem. Neurosci 2017, 8 (3), 513–523. [PubMed: 28045247]

(49). Storace DA; Cohen LB Measuring the olfactory bulb input-output transformation reveals a contribution to the perception of odorant concentration invariance. Nat. Commun 2017, 8 (1), 81. [PubMed: 28724907]

(50). Yang F; Moss LG; Phillips GN, Jr The molecular structure of green fluorescent protein. Nat. Biotechnol 1996, 14 (10), 1246–1251. [PubMed: 9631087]

(51). Martelli C; Storace DA Stimulus Driven Functional Transformations in the Early Olfactory System. Front. Cell. Neurosci 2021, 15, 684742. [PubMed: 34413724]

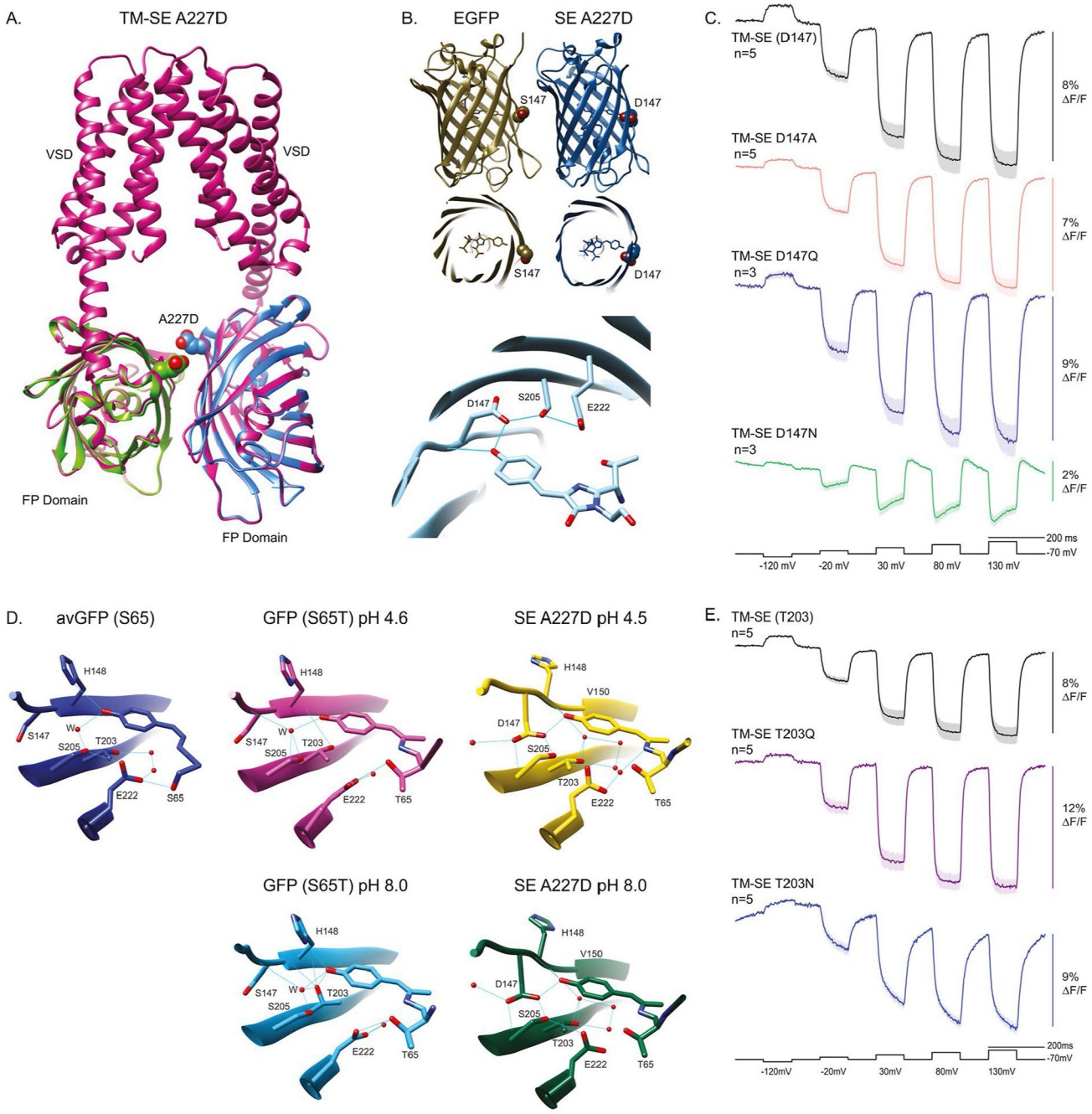

Figure 1.

Crystal structure of SE A227D reveals a conduit between the chromophore and the external surface of the β-can. (A) Schematic illustrating how membrane potential transients may influence FP fluorescence via dimerization of voltage-sensing domains (VSDs) in an ArcLight-derived GEVI (TM). The pink model shows a predicted VSD dimer generated using AlphaFold 3,31 while overlaid green and blue structures represent SE crystal structures solved at pH 8. The A227D mutation, located on the FP's external surface, is marked by spheres; red atoms indicate aspartate oxygens. The VSD dimer interface has

not been experimentally validated this schematic is for illustration only. (B) Comparison of SE A227D and EGFP (PDB: 4EUL24) structures. Side view of SE A227D highlights the D147 side chain, introduced during SE development, spanning from the chromophore interior to the protein surface one oxygen forms a hydrogen bond with the chromophore while the other remains solvent-exposed. The lower panel depicts a proton wire connecting the chromophore to E222 via D147 and S205. A top-down view emphasizes D147's axial span across the β-can. SE A227D structures were nearly identical across pH conditions (see Supplemental Figure S1). (C) Mutagenesis at position D147 reveals a limited influence on the voltage-dependent optical signal, suggesting that D147 is not directly involved in responding to the neighboring A227D charge during voltage-induced fluorescence changes. GEVIs carrying D147X mutations were expressed in HEK293 cells and imaged under whole-cell voltage clamp. Dark traces represent mean fluorescence responses of all cells tested; shaded regions indicate standard error of the mean (SEM). Voltage steps are shown below each trace. "n" refers to the number of cells recorded. Each cell was subjected to four trials with each trial consisting of four repetitions of the voltage protocol (black trace). An offline, lowpass Butterfield 100 Hz filter was applied to the traces. The sampling rate was 1 kHz. Other D147X mutations are shown in Supplemental Figure S2). (D) Structural comparison of chromophore-adjacent hydrogen bond networks in avGFP (PDB: 1GFL50), GFP(S65T) at low and high pH (PDBs: 1C4F, 1EMG25), and SE A227D. In SE A227D, D147 replaces a water molecule in the proton wire, maintaining chromophore contact across pH (Supplemental Figure S1). This is enabled by a shift in the seventh β-strand start site (V150), which positions H148 on the exterior, making space for D147 to orient inward. Despite the presence of T65 in the chromophore, the proton wire to E222 remains intact in SE A227D. In contrast, GFP(S65T) shows a disrupted wire and pH-dependent T203 rotation. For avGFP, the proton wire exists from the chromophore to a water molecule to S205 to E222. For GFP (S65T), E222 is rotated terminating the hydrogen bond between S205 and E222. For SE A227D, the proton wire exists from the chromophore to D147 to S205 to E222. (E) Mutations at T203 alter the kinetics of the voltage-dependent fluorescence response, suggesting conformational changes near the chromophore. T203X variants were expressed in HEK293 cells and imaged under voltage clamp, revealing distinct kinetic profiles across constructs consistent with dynamic chromophore environment modulation. Experimental conditions as in C.

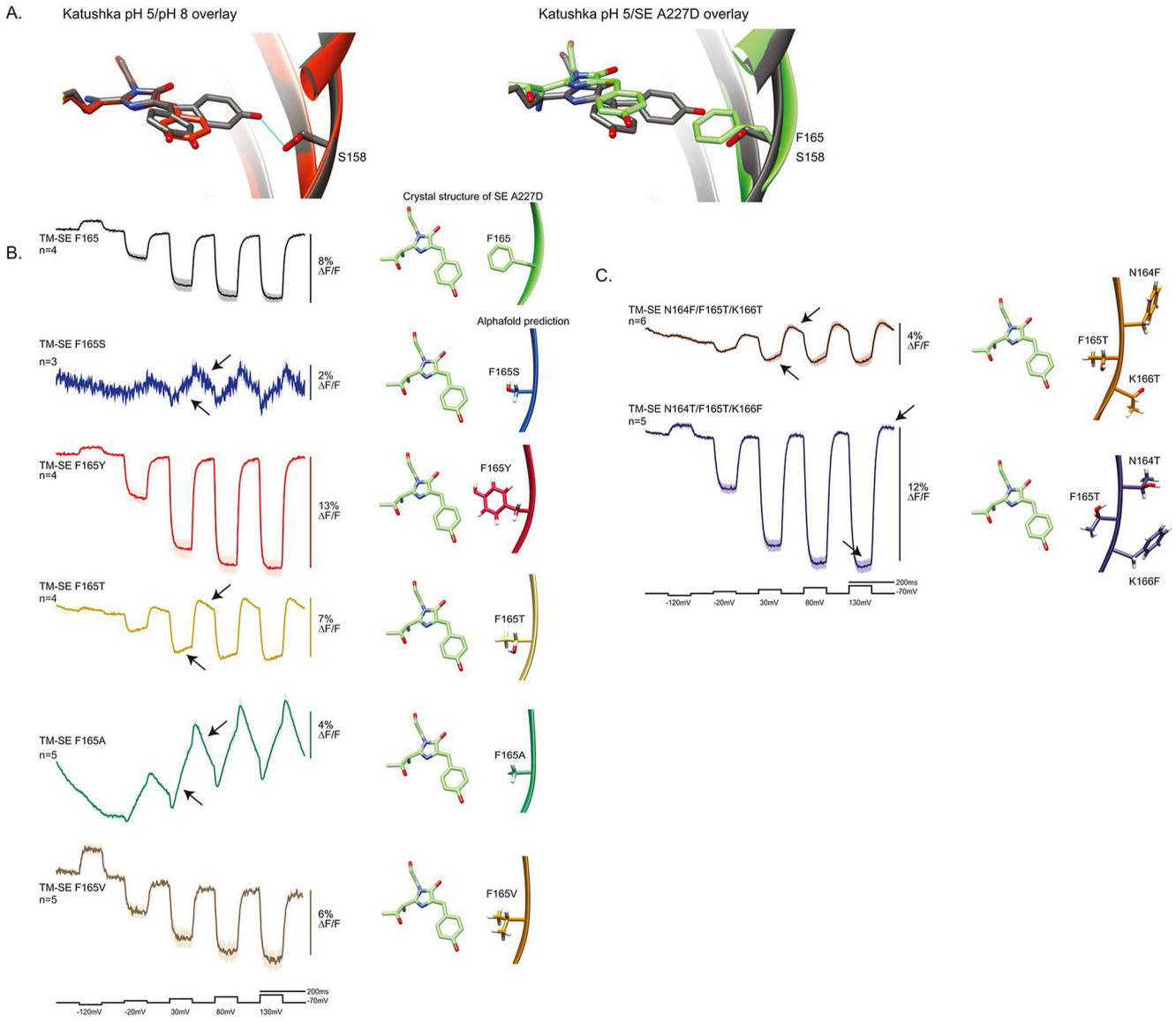

Figure 2.

Observing chromophore flexibility by disrupting steady-state fluorescence. (A) Structural comparison between Katushka30 and SE A227D illustrates how local environment influences chromophore mobility. Left: Overlay of Katushka chromophore structures at pH 5.5 (gray) and pH 8.0 (red) reveals a pH-dependent cis-to-trans rotation associated with increased brightness at alkaline pH. Right: Katushka (dim, pH 5.5) overlaid with SE A227D (green). The Katushka chromophore in the trans configuration forms a hydrogen bond with S158 of the β-can, but the homologous position in SE A227D, F165, sterically blocks this interaction, limiting chromophore rotation. (B) Mutations at position 165 reveal a secondary voltage-dependent component consistent with increased chromophore flexibility. HEK293 cells expressing GEVI constructs with F165X substitutions were imaged under whole-cell voltage clamp. Cells were held at −70 mV and subjected to voltage steps as indicated by the trace below each panel. Solid lines represent mean responses; shaded areas indicate SEM

(N = number of cells; 16 repetitions per cell). Traces were acquired at 1 kHz and processed with a 100 Hz low-pass Butterworth filter unless otherwise noted. To the right of each trace, AlphaFold-predicted side chain conformations are overlaid on the SE A227D crystal structure (pH 8.0). Arrows denote secondary components in the fluorescence response. (C) External modulation of electric permittivity can restore chromophore rigidity. Constructs with directionally polarized flanking residues SE N164F/F165T/K166T (FTT) and SE N164T/F165T/K166F (TTF) were expressed in HEK293 cells and tested under identical voltage clamp conditions as in (B). Reversing the external polarity offset (TTF) eliminated the secondary component, consistent with restored steric hindrance at the chromophore.

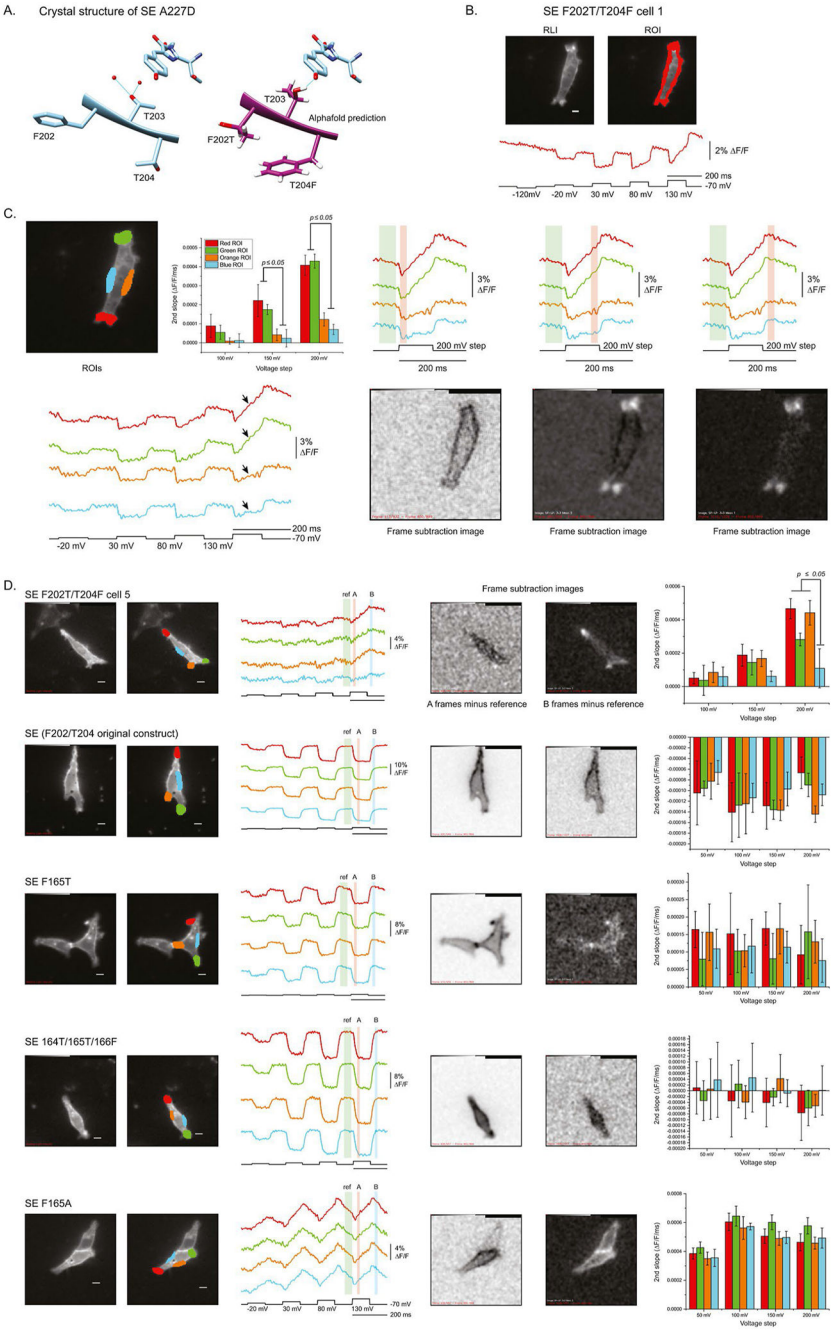

Figure 3.

A second threonine switch reveals an influence of membrane curvature on protein activity. (A) Structural comparison shows that the orientation of T203 is potentially sensitive to the external amino acid context at positions 202 and 204. Left: crystal structure of SE A227D at pH 8.0 showing T203 in its native orientation. Right: AlphaFold prediction of the F202T/T204F mutant overlaid onto the SE A227D structure reveals an alternative T203 conformation that permits hydrogen bonding (blue line) with the chromophore. (B) Prototypical voltage-dependent fluorescence response from an HEK293 cell expressing

TM-SE F202T/T204F. Depolarizing steps of increasing amplitude result in a progressively enhanced secondary optical component. The fluorescence trace was extracted from a whole-cell ROI (red outline). (C) The TM-SE F202T/T204F mutant exhibits a curvature-dependent secondary fluorescence component during voltage steps. ROIs from curved versus flatter plasma membrane regions revealed enhanced secondary transitions in curved areas. Optical traces (color-coded to ROIs) represent the average of 16 repetitions (4 trials × 4 sweeps). Arrows indicate the increased secondary voltage-dependent response. The secondary component in each trial was quantified by linear fitting of the trace from 40 ms after depolarization until 1 ms before repolarization (bar graph, “2nd slope”). Statistical significance was assessed by two-way ANOVA with a post hoc Scheffe test. Frame-subtraction images (early, late, and poststimulus red shaded frames) during a 200 mV depolarization step show that all membrane regions initially dim, but curved regions subsequently brighten, producing a steeper secondary component. Dark pixels indicate decreased fluorescence relative to reference frames (green shading), while light pixels represent increased signal. (D) In contrast, F165X mutants display a uniform voltage-dependent response across membrane regions. The top cell (another SE F202T/T204F example) illustrates curvature-sensitive responses, whereas F165X constructs lacked such variability (see Supplemental Figures S4 and S5). Traces and bar graphs are presented as in (C), with frame-subtraction images aligned to the shaded reference periods.

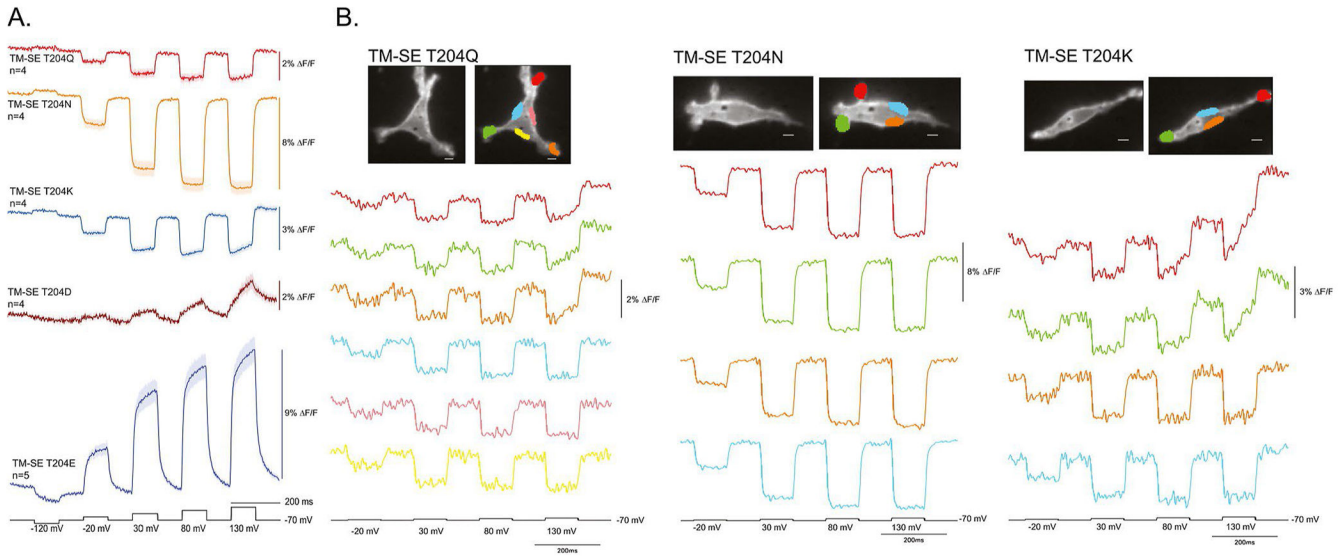

Figure 4.

Side chain charge and orientation at the external 204 position influence the voltage-dependent optical signal. (A) Voltage-dependent optical responses from HEK293 cells expressing GEVI constructs with T204 mutations. Cells were subjected to membrane depolarization steps indicated by the black trace below each fluorescence signal. Solid lines represent the mean of 16 trials; shaded regions show the standard error of the mean (SEM). All recordings were low-pass filtered offline at 100 Hz. Fluorescence traces were extracted from ROIs encompassing the entire plasma membrane. (B) Membrane curvature modulates the voltage-dependent fluorescence response for the T204Q and T204K constructs but not for T204N. Representative single-cell examples are shown for each mutant. Left: resting fluorescence images. Right: corresponding images with ROIs drawn over subregions of the plasma membrane. Below: fluorescence traces from the labeled ROIs. Curvature-sensitive secondary components were observed for T204Q and T204 K, but not for T204N (Supplemental Figures S7 and S8).

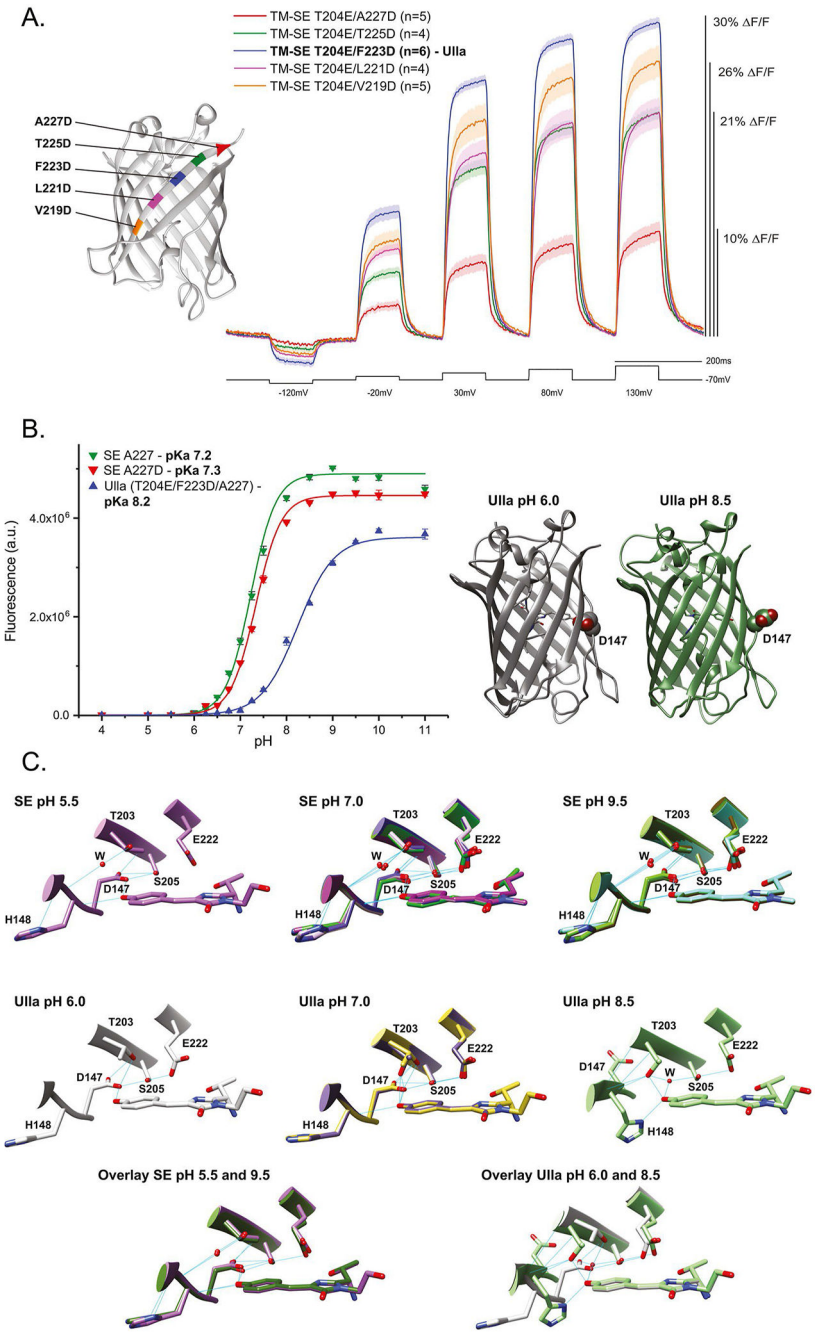

Figure 5.

Influencing the orientation of T203 through external mutations creates a novel GEVI with a shifted pH sensitivity. (A) Aspartic acid scan of surface residues along the 11th β-strand reveals that repositioning the external negative charge influences the voltage-dependent fluorescence signal. In each construct, the original A227D mutation was reverted to alanine, and an aspartic acid was introduced at one of four alternate positions: T225D(green), F223D (blue), L221D (pink), or V219D (orange). All constructs included the T204E mutation. (B) The FP domain of the novel GEVI, Ulla (T204E/F223D), exhibits an alkaline-shifted

pKa relative to SE and SE A227D. All three FPs were purified from bacteria and assessed across a range of pH values. Fluorescence increased with pH for each construct, but Ulla displayed a pKa of ~8.2 outside the physiological range indicating reduced pH sensitivity under normal cellular conditions. (C) External mutations in Ulla (T204E/F223D) alter the orientation and flexibility of internal side chains near the chromophore, particularly T203 and D147. FP domains from Ulla and SE were crystallized at different pH values and compared structurally. At pH 6.0 (below Ulla's pKa), the configuration resembles SE and SE A227D: D147 spans from the external surface to the chromophore, forming a hydrogen bond. At pH 8.5, three of the four Ulla structures show extension of the seventh β-strand, fully repositioning D147 to the external surface. A water molecule (W) replaces the internal hydrogen bond, and H148 rotates inward to interact with the chromophore. The fourth unit retains the lower-pH configuration (PDB: 8JLU). Top row: SE structures at pH 5.5, 7.0, and 9.5. One representative unit of SE at pH 5.5 while pH 7.0 and 9.5 include overlays of all four crystallized units. Bottom row: Ulla structures at pH 6.0 (single unit), pH 7.0 (overlay of two units), and pH 8.5 (overlay of four units). At higher pH, T203 in Ulla adopts multiple rotameric states, reflecting increased internal flexibility. Hydrogen bonds are shown as blue lines. Oxygen atoms are in red; nitrogen atoms in blue.

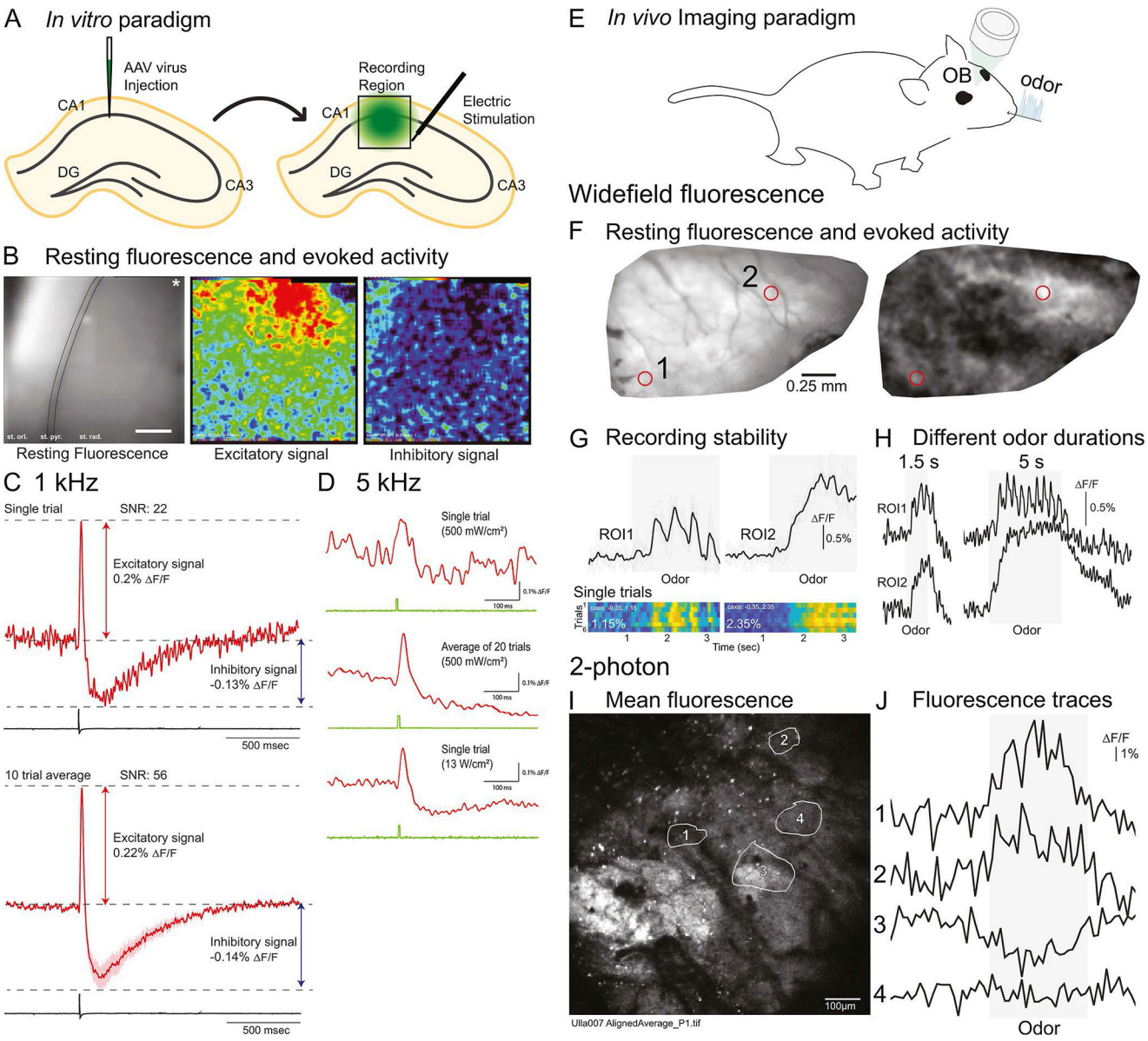

Figure 6.

Ex vivo and in vivo population recordings using Ulla. (A) Schematic of the ex vivo experimental setup showing acute brain slice recordings from the CA1 region of the mouse hippocampus. Ulla was expressed via AAV under the control of the synapsin promoter and imaged at 1 kHz. (B) Electrical stimulation of the Schaffer collaterals (black trace in fluorescence panel) evoked a fluorescence increase corresponding to membrane depolarization, followed by a decrease reflecting inhibitory activity. The stimulation site is marked by an asterisk in the resting fluorescence image. Scale bar is 100 µm. (C,D) Recordings from hippocampal slices at 1 kHz and 5 kHz under varying illumination intensities. Experimental design is as in (A). (C) Fluorescence responses at 1 kHz under standard light conditions. (D) At 5 kHz, a voltage response could still be detected under minimal excitation light (500 mW/cm2, top trace), with improved signal-to-noise ratio

(SNR) upon trial averaging or increased illumination (13 W/cm2, bottom trace). (E) Schematic of the in vivo imaging setup targeting the dorsal olfactory bulb in anesthetized mice (adapted from Martelli & Storace, 202151). (F–H) In vivo widefield imaging of odor-evoked responses. (F) Left: mean baseline fluorescence image. Right: ΔF frame subtraction map showing spatial activation in response to odor (methyl valerate). Red ROIs indicate regions of interest used for time-course analysis. (G) Top: mean fluorescence time courses from two distinct ROIs. Bottom: single-trial traces show trial-to-trial consistency. (H) Fluorescence responses from the same ROIs under different odor stimulation durations (1.5 s vs 5 s) reveal respiratory-locked oscillations and distinct temporal dynamics. (I,J) Two-photon imaging of odor-evoked activity in the dorsal olfactory bulb. (I) Mean fluorescence image generated from an average of 13 trials, revealing localized glomerular activity. (J) Fluorescence time courses from four ROIs during a 1.5 s odor presentation. Traces represent the average of 13 respiration-aligned trials, capturing stimulus-locked dynamics.